

Article

Shape Effects of Ceria Nanoparticles on the Water-Gas Shift Performance of $\text{CuO}_x/\text{CeO}_2$ Catalysts

Maria Lykaki ¹, Sofia Stefa ¹, Sónia A. C. Carabineiro ^{2,3} , Miguel A. Soria ⁴ , Luís M. Madeira ⁴ 
and Michalis Konsolakis ^{1,*} 

¹ School of Production Engineering and Management, Technical University of Crete, GR-73100 Chania, Greece; mlykaki@isc.tuc.gr (M.L.); sstefa@isc.tuc.gr (S.S.)

² LAQV-REQUIMTE, Department of Chemistry, NOVA School of Science and Technology, Universidade NOVA de Lisboa, 2829-516 Caparica, Portugal

³ Laboratory of Catalysis and Materials (LCM), Associate Laboratory LSRE-LCM, Faculty of Engineering, University of Porto, 4200-465 Porto, Portugal; sonia.carabineiro@fct.unl.pt

⁴ LEPABE—Laboratory for Process Engineering, Environment, Biotechnology and Energy, Faculty of Engineering, University of Porto, Rua Dr. Roberto Frias, 4200-465 Porto, Portugal; masoria@fe.up.pt (M.A.S.); mmadeira@fe.up.pt (L.M.M.)

* Correspondence: mkonsol@pem.tuc.gr; Tel.: +30-28210-37682

Abstract: The copper–ceria ($\text{CuO}_x/\text{CeO}_2$) system has been extensively investigated in several catalytic processes, given its distinctive properties and considerable low cost compared to noble metal-based catalysts. The fine-tuning of key parameters, e.g., the particle size and shape of individual counterparts, can significantly affect the physicochemical properties and subsequently the catalytic performance of the binary oxide. To this end, the present work focuses on the morphology effects of ceria nanoparticles, i.e., nanopolyhedra (P), nanocubes (C), and nanorods (R), on the water–gas shift (WGS) performance of $\text{CuO}_x/\text{CeO}_2$ catalysts. Various characterization techniques were employed to unveil the effect of shape on the structural, redox and surface properties. According to the acquired results, the support morphology affects to a different extent the reducibility and mobility of oxygen species, following the trend: $R > P > C$. This consequently influences copper–ceria interactions and the stabilization of partially reduced copper species (Cu^+) through the $\text{Cu}^{2+}/\text{Cu}^+$ and $\text{Ce}^{4+}/\text{Ce}^{3+}$ redox cycles. Regarding the WGS performance, bare ceria supports exhibit no activity, while the addition of copper to the different ceria nanostructures alters significantly this behaviour. The $\text{CuO}_x/\text{CeO}_2$ sample of rod-like morphology demonstrates the best catalytic activity and stability, approaching the thermodynamic equilibrium conversion at 350 °C. The greater abundance in loosely bound oxygen species, oxygen vacancies and highly dispersed Cu^+ species can be mainly accounted for its superior catalytic performance.

Keywords: ceria nanoparticles; $\text{CuO}_x/\text{CeO}_2$ mixed oxides; shape effects; water–gas shift reaction (WGSR)



Citation: Lykaki, M.; Stefa, S.; Carabineiro, S.A.C.; Soria, M.A.; Madeira, L.M.; Konsolakis, M. Shape Effects of Ceria Nanoparticles on the Water-Gas Shift Performance of $\text{CuO}_x/\text{CeO}_2$ Catalysts. *Catalysts* **2021**, *11*, 753. <https://doi.org/10.3390/catal11060753>

Academic Editor: Leonarda Francesca Liotta

Received: 25 May 2021

Accepted: 18 June 2021

Published: 21 June 2021

Publisher's Note: MDPI stays neutral with regard to jurisdictional claims in published maps and institutional affiliations.



Copyright: © 2021 by the authors. Licensee MDPI, Basel, Switzerland. This article is an open access article distributed under the terms and conditions of the Creative Commons Attribution (CC BY) license (<https://creativecommons.org/licenses/by/4.0/>).

1. Introduction

Hydrogen production is considered an interesting alternative in the overall energy demand scheme. Concerning the hydrogen economy, polymer electrolyte membrane fuel cells (PEMFCs) ought to play a major role in future years [1–3]. In this regard, it is important that CO impurities are eliminated in order for the anode electrodes to be protected. Hence, the water–gas shift (WGS: $\text{CO} + \text{H}_2\text{O} \leftrightarrow \text{CO}_2 + \text{H}_2$) is a reaction of particular importance in various reforming processes towards the production of hydrogen-rich gas streams for numerous applications [4].

Several catalysts have been employed so far for WGS [1]. Traditionally, copper–zinc and iron–chromium catalysts are employed for the low- and high-temperature WGS processes, respectively [2,5], exhibiting, however, various disadvantages, such as poor catalytic performance and strict pretreatment protocols, among other things [6]. Therefore, the research efforts are currently being focused on the facile preparation of more active and stable catalysts for WGS.

Ceria (CeO_2) has been broadly examined in many catalytic reactions, given its remarkable redox properties, high oxygen storage capacity (OSC) and oxygen mobility, as well as its improved thermal stability [7,8]. The fine-tuning of the shape and size of ceria towards the production of catalytic materials with certain textural and structural features can have a significant influence on redox and surface properties with great implications in catalytic performance [7,9–15].

More importantly, by combining ceria with various transition metals, the catalytic performance can be significantly enhanced, due to the synergistic metal–support interactions [16–19]. To this end, the copper–ceria catalytic system has been extensively investigated in heterogeneous catalysis due to its low cost, in comparison to noble metal-based catalysts, as well as its unique catalytic properties. The superior catalytic performance of this binary system can be mainly ascribed to the synergy between the two oxide components, as it has been comprehensively reviewed by Konsolakis [19]. In view of the above, the rational design of $\text{CuO}_x/\text{CeO}_2$ mixed oxides, e.g., on the basis of shape/size fine-tuning, alkali promotion, etc., can tremendously affect metal sites' local environment and in turn the metal–support interfacial reactivity [20]. In this regard, DFT calculations showed that doping the Cu(111) surface with boron (B) single atoms can adjust the active sites' local coordination environment, reducing the barrier of activation energy of the rate-determining step during WGS [21].

Regarding the $\text{CuO}_x/\text{CeO}_2$ catalyzed WGS reaction, two mechanisms were suggested, i.e., the redox or regenerative and the associative or formate mechanism [22–24]. In the first mechanism, CO adsorbs on copper and gets oxidized by ceria's oxygen, followed by support re-oxidation by H_2O . In the second one, CO is adsorbed on metal sites and reacts with the surface hydroxyl groups on ceria, followed by the intermediate (formate) decomposition to hydrogen and carbon dioxide [22–24]. In a recent study of Chen et al. [23], it was found that the interfacial perimeter is closely interrelated with the catalytic activity, with the chemical environment of $\text{Cu}^+-\text{O}_v-\text{Ce}^{3+}$ being involved in the low-temperature WGS. Moreover, the tightly attached Cu-[O_x]-Ce species, likely linked to ceria's oxygen vacancies, were shown to be the active species by Flytzani-Stephanopoulos and colleagues [25], with the CuO_x nanoparticles and the weakly bound copper oxide clusters behaving as spectators. In this respect, the activation of water at the Cu–Ce interface is thought to be the rate-determining step [23,26]. In a similar manner, the superior CO oxidation performance of $\text{CuO}_x/\text{CeO}_2$ nanorods, as compared to nanopolyhedra and nanocubes, was recently revealed, which is mainly ascribed to their abundance in oxygen defects as well as to the synergistic interfacial interactions [27].

The key role of support morphology in the WGS activity of $\text{CuO}_x/\text{CeO}_2$ catalysts was demonstrated by employing different nanoceria shapes, such as spheres, rods, cubes and octahedra [28,29]. In particular, Ren et al. [28] investigated the impact of CeO_2 morphology (nanooctahedrons, nanorods, nanocubes) on the WGS activity of $\text{CuO}_x/\text{CeO}_2$ catalysts, revealing the superiority of nanooctahedrons in comparison to the other nanostructures, due mainly to their abundance in CuO_x species interacting strongly with ceria. In a similar manner, Yao et al. [29] explored the effect of support morphology (nanospheres, nanorods, nanocubes) on the WGS performance of $\text{CuO}_x/\text{CeO}_2$ catalysts, demonstrating the superiority of nanospheres, owing to their abundance in defects and imperfections favouring strong metal–support interactions. In general, different ceria nanoshapes exhibit different defect chemistry, leading to diverse behaviour during the interaction with CO and water [30]. It should also be mentioned that the shape of copper can significantly affect the

WGS activity. For instance, it was revealed that copper in a cubic shape exhibited higher WGS activity than that in an octahedral shape [31].

Despite the extensive work in the field, no definitive conclusions have been drawn in relation to the influence of ceria shape on the redox properties and WGS activity of $\text{CuO}_x/\text{CeO}_2$ catalysts. The latter is mainly attributed to the fact that besides the support morphology, various other factors, such as metal loading, synthesis procedure and pretreatment protocols can notably affect the intrinsic reactivity and metal–support interactions [19,20,32].

In view of these aspects and motivated by our previous experience in the field of ceria shape effects in catalysis [27,32], we extended our research efforts to WGS reaction. In particular, three different ceria nanoshapes (polyhedra, cubes and rods) were hydrothermally prepared and used as supports for the copper oxide phase. A thorough characterization study was performed, including N_2 adsorption-desorption at -196°C , X-ray diffraction, transmission electron microscopy, H_2 -temperature programmed reduction, inductively coupled plasma atomic emission spectroscopy, X-ray photoelectron spectroscopy and UV-Vis spectroscopy, to obtain information on the morphology effects of ceria nanostructures on surface chemistry and WGS activity of $\text{CuO}_x/\text{CeO}_2$ mixed oxides.

2. Results and Discussion

2.1. Morphological Characterization (TEM)

Transmission electron microscopy (TEM) images were obtained in order to explore the morphological characteristics of the as-prepared samples. Bare ceria supports are presented in Figure 1a–c. The formation of ceria nanoparticles of rod-like, polyhedral and cubic shape through the hydrothermal method is evident in Figure 1a–c, respectively. Particularly, the length of the rods varies between 25 and 200 nm and their width ranges from 10 to 18 nm. Ceria nanopolyhedra demonstrate irregular shapes with their sizes varying between 5 and 11 nm, while the size of ceria nanocubes ranges from 15 to 30 nm. The TEM images of $\text{CuO}_x/\text{CeO}_2$ materials are depicted in Figure 1d–f; higher-magnification images are also shown in Figure 1g–i. Obviously the support morphology remains unaffected by copper addition into ceria carriers, whereas no agglomeration of the different phases is evident. These findings are in accordance with the XRD results, as further discussed below.

2.2. Structural and Textural Characterization (XRD/BET)

The structural and textural properties of the samples are summarized in Table 1. Bare ceria materials exhibit larger BET surface areas, as compared to the mixed ones, following the order: CeO_2 (P) ($109\text{ m}^2/\text{g}$) > CeO_2 (R) ($92\text{ m}^2/\text{g}$) > CeO_2 (C) ($40\text{ m}^2/\text{g}$). Incorporating copper into ceria supports (through impregnation and subsequent calcination) reduces the BET surface area in all samples, with nanopolyhedra still exhibiting the highest value. Specifically, the copper–ceria samples demonstrate the following sequence in relation to surface area: Cu/CeO_2 (P) ($91\text{ m}^2/\text{g}$) > Cu/CeO_2 (R) ($75\text{ m}^2/\text{g}$) > Cu/CeO_2 (C) ($34\text{ m}^2/\text{g}$).

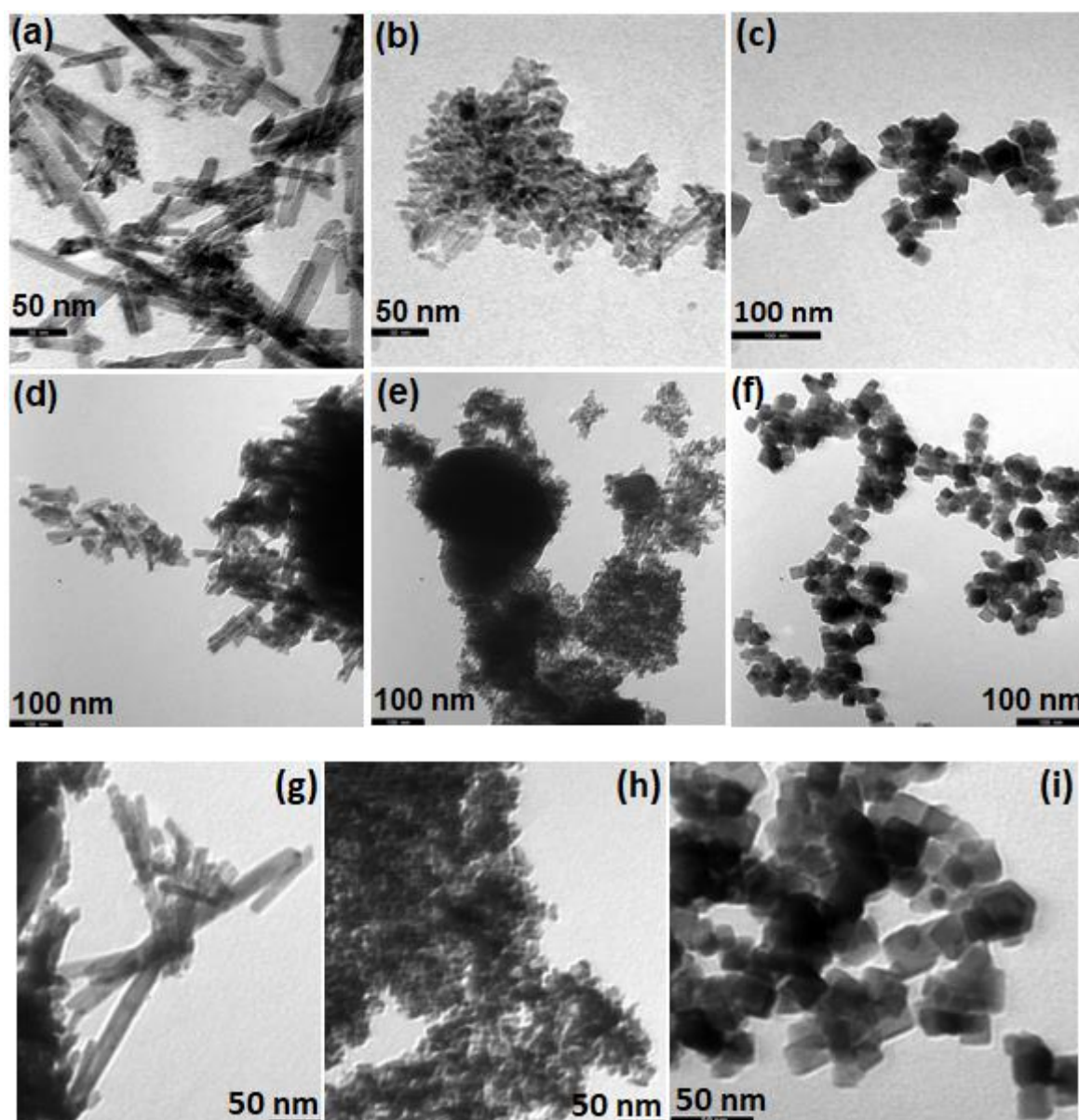


Figure 1. TEM results of as-prepared materials: (a) CeO₂ (R), (b) CeO₂ (P), (c) CeO₂ (C), (d,g) Cu/CeO₂ (R), (e,h) Cu/CeO₂ (P) and (f,i) Cu/CeO₂ (C).

Table 1. Structural and textural properties of pure CeO₂ and CuO_x/CeO₂ samples.

Sample	N ₂ Adsorption-Desorption			XRD	
	BET Surface Area (m ² /g)	Pore Volume (cm ³ /g)	Average Pore Size (nm)	Average Crystallite Diameter, D _{XRD} (nm) ¹	
				CeO ₂	CuO
CeO ₂ (C)	40	0.12	12.5	19.2	-
CeO ₂ (R)	92	0.71	30.9	13.2	-
CeO ₂ (P)	109	1.04	38.1	9.5	-
Cu/CeO ₂ (C)	34	0.29	33.4	19.2	52
Cu/CeO ₂ (R)	75	0.40	21.2	11.6	43
Cu/CeO ₂ (P)	91	0.29	12.7	9.6	31

¹ Calculated applying Scherrer's equation (Equation (3) in the "Materials Characterization" section).

Figure 2a shows the pore size distribution (PSD) of pure ceria and $\text{CuO}_x/\text{CeO}_2$ samples. In all cases, maxima at pore diameters higher than 3 nm are obtained, indicating the mesoporosity of the as-prepared samples [33]. As is obvious from the adsorption–desorption isotherms (Figure 2b), the materials demonstrate type IV isotherms with a hysteresis loop at a relative pressure >0.5 , further confirming the mesoporous structure of the materials [34,35]. As shown in Table 1, the addition of copper reduces the pore volume and the average pore size for nanorods (R) and nanopolyhedra (P), while an increase in these values is observed for nanocubes (C). The CeO_2 (P) sample possesses the highest average pore size (38.1 nm), followed by CeO_2 (R) (30.9 nm) and CeO_2 (C) (12.5 nm). Regarding the $\text{CuO}_x/\text{CeO}_2$ samples, a different trend is observed, as the Cu/CeO_2 (C) sample exhibits the highest average pore size (33.4 nm), followed by Cu/CeO_2 (R) (21.2 nm) and Cu/CeO_2 (P) (12.7 nm). The observed differences in pore features in conjunction to the crystallite size of CuO and CeO_2 phases (Table 1) can be mainly considered for the observed differences in S_{BET} , as further discussed below.

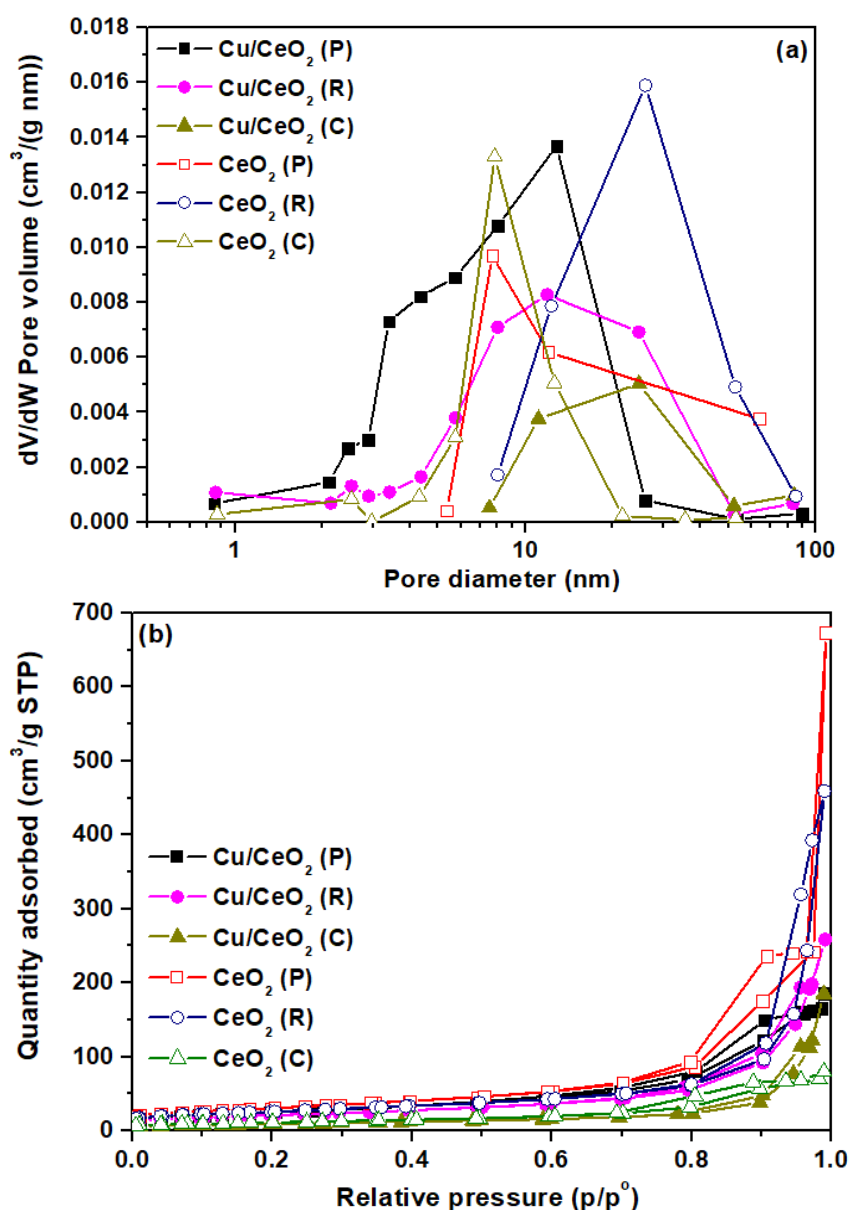


Figure 2. (a) The BJH (Barret-Joyner-Halenda) desorption pore size distribution (PSD) and (b) the adsorption–desorption isotherms of pure CeO_2 and $\text{CuO}_x/\text{CeO}_2$ samples of different morphology.

The XRD diffractograms of as-prepared samples are depicted in Figure 3. The main peaks can be indexed to (111), (200), (220), (311), (222), (400), (331) and (420) planes of a ceria face-centred cubic fluorite structure (Fm3m symmetry, no. 225) [36]. The mixed oxides exhibit XRD peaks at $2\theta = 35.3^\circ$, 38.2° and 62° , which are attributed to CuO crystal phase. The peaks observed at $2\theta = 42\text{--}44^\circ$ in the Cu/CeO₂ (C) sample are attributed to interferences from the stainless-steel sample holder. Scherrer's equation (Equation (3)) was applied, within the approximation degree induced by the method, for the evaluation of the primary crystallite size of CuO and CeO₂ phases (Table 1). The mean particle size of ceria is 19.2, 13.2 and 9.5 nm for CeO₂ (C), CeO₂ (R) and CeO₂ (P), respectively, being in the range of TEM analysis (Figure 1). It is worth mentioning that adding CuO into CeO₂ does not alter its main features (see TEM analysis above), with ceria's mean particle size remaining almost unchanged in nanocubes and nanopolyhedra, while it changes slightly in nanorods. Regarding the average size of CuO, it follows the order: Cu/CeO₂ (C) (52 nm) > Cu/CeO₂ (R) (43 nm) > Cu/CeO₂ (P) (31 nm), which coincides with the order of bare ceria. It should be also noted that the crystallite size of both CuO and CeO₂ follows the reverse order of the BET surface area (Table 1).

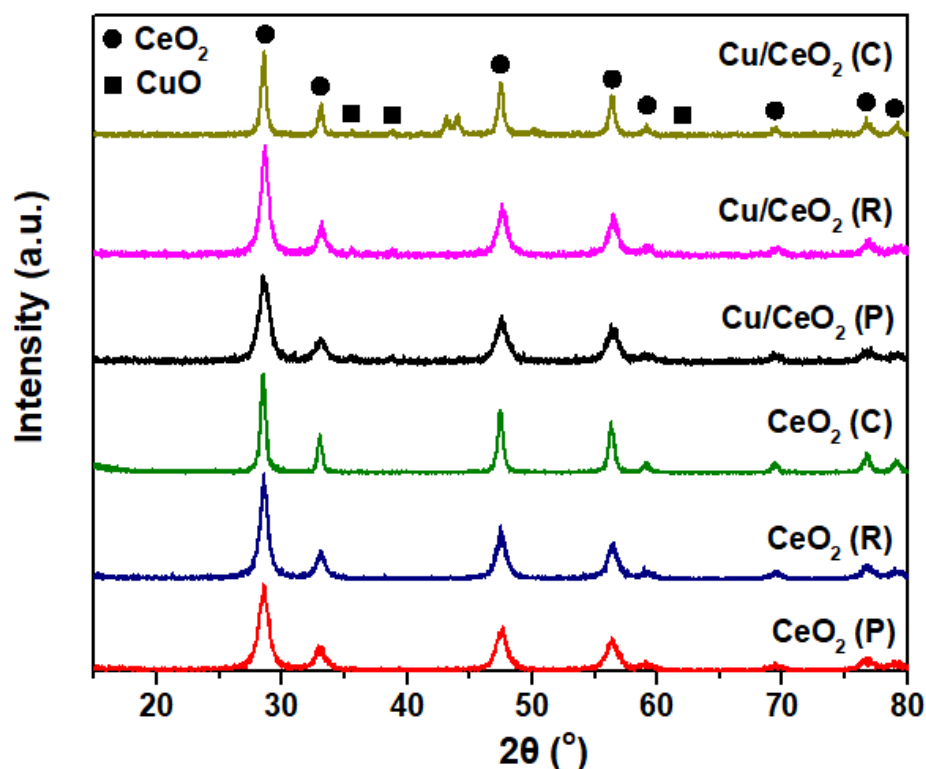


Figure 3. XRD diffractograms of pure CeO₂ and CuO_x/CeO₂ samples.

2.3. Electronic Properties (UV-Vis)

To better understand the electronic states and coordination environment of the materials, UV-Vis spectroscopy was performed. Figure 4 depicts the UV-Vis spectra as well as the band gap energy of bare ceria nanoparticles. In particular, two bands at ~286 nm and 344 nm are found, corresponding to the O²⁻ to Ce⁴⁺ charge transfer and inter band transitions, respectively [28,37]. In terms of band gap, the following order is acquired for single ceria nanoparticles of different morphology: CeO₂ (P) (2.99 eV) < CeO₂ (R) (3.02 eV) < CeO₂ (C) (3.14 eV). Ceria nanocubes exhibit the highest band gap energy value, whereas the other two ceria nanostructures (polyhedra and rods) show similar values. The latter could be related with the inferior reducibility and oxygen mobility of ceria nanocubes, as compared to the other morphologies, as further discussed below. In this respect, it has been reported that low band gap energy values of ceria nanoparticles could be linked with

their abundance in oxygen vacancies and partially reduced Ce^{3+} species [38]. The latter is further verified in the present work on the basis of XPS analysis (*vide infra*).

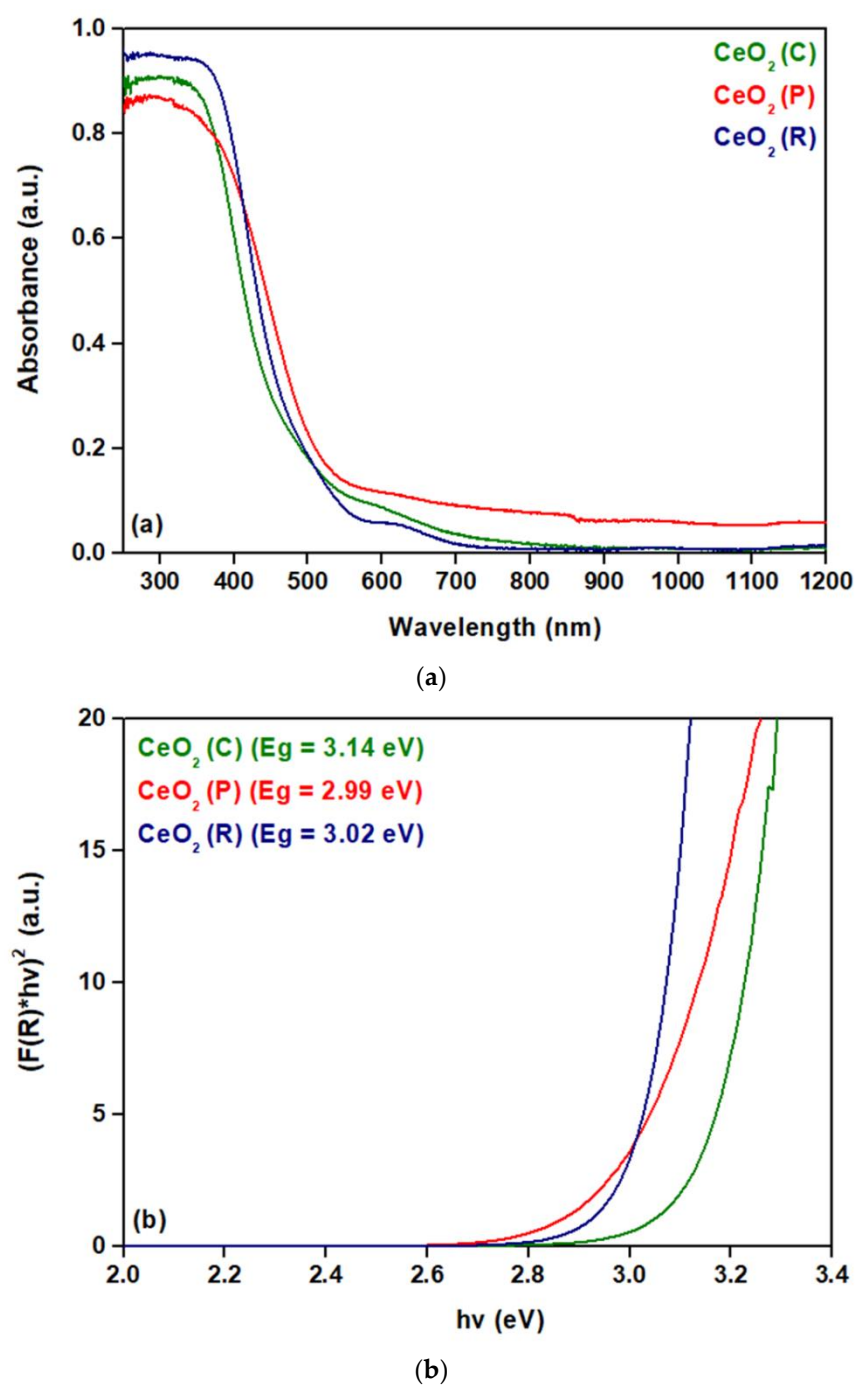


Figure 4. (a) Absorbance spectra and (b) $(F(R)*hv)^2$ diagram as a function of photon energy based on Kubelka-Munk model for ceria samples of different morphology (nanocubes (C), nanopolyhedra (P), nanorods (R)).

2.4. Redox Properties (H_2 -TPR)

The morphological effects of CeO_2 on reducibility were explored by TPR experiments, using H_2 as reducing gas. The reduction profiles of pure CeO_2 and CuO_x/CeO_2 samples are shown in Figure 5. The quantitative results, in terms of H_2 consumption ($mmol H_2/g$) and TPR peak temperature, are summarized in Table 2. Pure ceria exhibits two broad peaks at ca. $550\text{ }^\circ C$ (O_s) and $800\text{ }^\circ C$ (O_b), corresponding to the reduction of surface and bulk oxygen, respectively [39,40]. The reduction profile of bare CuO , included for comparison purposes, exhibits one reduction peak at $380\text{--}390\text{ }^\circ C$.

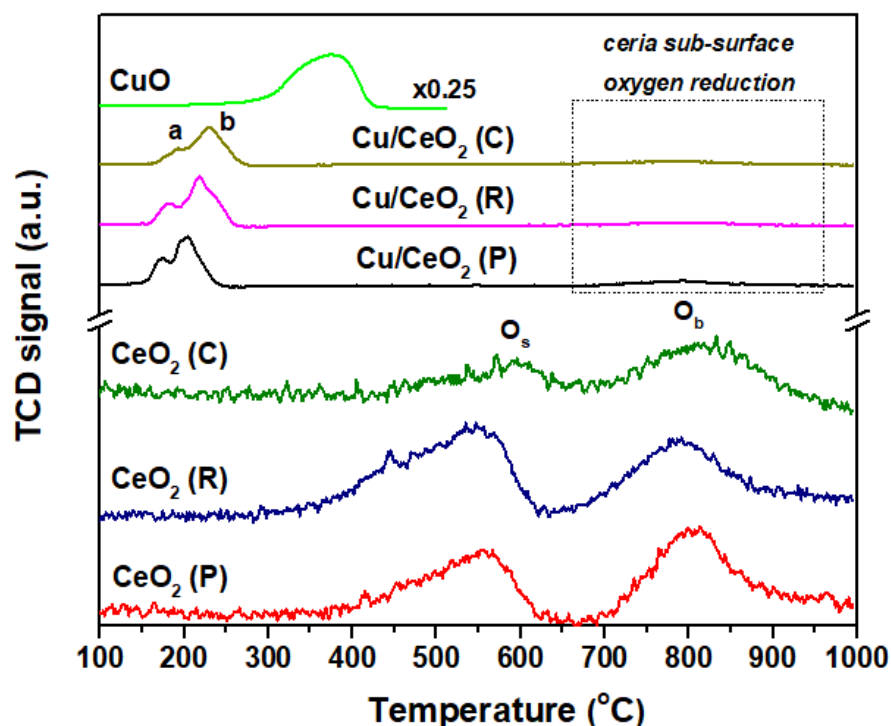


Figure 5. H_2 -TPR profiles of pure ceria, CuO , and CuO_x/CeO_2 materials.

Table 2. Redox properties of pure CeO_2 and CuO_x/CeO_2 samples.

Sample	H_2 Consumption ($mmol H_2/g$) ¹	TPR Peak Temperature ($^\circ C$)	
CeO_2 (C)	0.41	589	809
CeO_2 (R)	0.59	545	788
CeO_2 (P)	0.48	555	804
Cu/CeO_2 (C)	1.50	194	228
Cu/CeO_2 (R)	1.80	181	217
Cu/CeO_2 (P)	1.65	176	201

¹ Estimated by the quantification of H_2 uptake in the $100\text{--}700\text{ }^\circ C$ range of the H_2 -TPR profiles.

Importantly, the reduction of mixed oxides takes place at significantly lower temperatures than pure CeO_2 and CuO , implying a synergistic interaction between copper and ceria, which leads to enhanced reducibility. In particular, mixed oxides show two reduction peaks at $176\text{--}228\text{ }^\circ C$ and one broad but less intense peak at ca. $793\text{ }^\circ C$, which is related to the reduction of ceria sub-surface oxygen [41]. The peak at lower temperatures around $176\text{--}194\text{ }^\circ C$ (peak a) is due to the reduction of finely dispersed CuO_x species strongly interacting with the surface of CeO_2 [42–44], whereas the peak at higher temperatures (peak b) can be related to larger CuO clusters formed on the surface of CeO_2 [45].

To provide a quantitative insight into the effect of ceria morphology and metal–support interactions on the redox characteristics of the mixed oxides, the hydrogen consumed in

the lower temperature interval, which is related to the reduction of ceria surface oxygen (O_s peak) and CuO_x species, was estimated in both pure ceria and CuO_x/CeO_2 materials (Table 2). Bare ceria nanorods exhibit the largest surface/bulk oxygen (O_s/O_b) ratio (1.13), followed by ceria nanopolyhedra (0.94) and ceria nanocubes (0.71), indicating that ceria nanorods possess the highest population in weakly bonded oxygen, which consequently enhances oxygen mobility and reducibility. At this point, it ought to be mentioned that these findings are in complete agreement with the abundant defects and oxygen vacancies of ceria nanorods, as recently confirmed by Raman analysis performed in our previous work [27]. Regarding the H_2 consumption of CuO_x/CeO_2 samples, the following sequence is obtained: Cu/CeO_2 (R) (1.80 mmol H_2/g) > Cu/CeO_2 (P) (1.65 mmol H_2/g) > Cu/CeO_2 (C) (1.50 mmol H_2/g), evidencing the superior reducibility of Cu/CeO_2 (R). Importantly, the hydrogen consumption of the mixed oxides surpasses the theoretical one (~1.34 mmol H_2/g for a nominal Cu loading of ca. 8.5 wt.%), implying that the reduction of CeO_2 capping oxygen is facilitated in the presence of copper, further corroborating the above arguments. At this point, it should be mentioned that ICP analysis in the CuO_x/CeO_2 samples revealed an actual copper loading of 8.4 ± 0.2 wt.% for all samples, which is very close to the nominal one (see Materials Synthesis).

2.5. Surface Analysis (XPS)

The morphological effect of ceria supports on the surface chemistry of pure CeO_2 and CuO_x/CeO_2 materials was evaluated by XPS analysis. Figure 6a depicts the XPS Ce 3d spectra, deconvoluted into eight components, comprising of the spin-orbit lines u and v, as clearly described in our previous work [27]. In brief, the u lines correspond to $Ce\ 3d_{3/2}$, with three peaks: u, u'' and u''' (at 900.7, 907.6 and 916.4 eV, respectively). The v lines ($Ce\ 3d_{5/2}$) include three peaks: v, v'' and v''' (at 882.2, 888.8, and 898.2 eV, respectively). The above-mentioned six peaks are due to Ce^{4+} , with the two remaining spectral lines (u' at 902.1 eV and v' at 883.8 eV) being characteristic of Ce^{3+} species. The ratio of Ce^{3+} to total cerium is obtained from the corresponding areas' ratio [43]. As seen in Table 3, CeO_2 (C) shows the lowest population of Ce^{3+} species, followed by CeO_2 (R) and CeO_2 (P), confirming the UV-Vis results (vide supra).

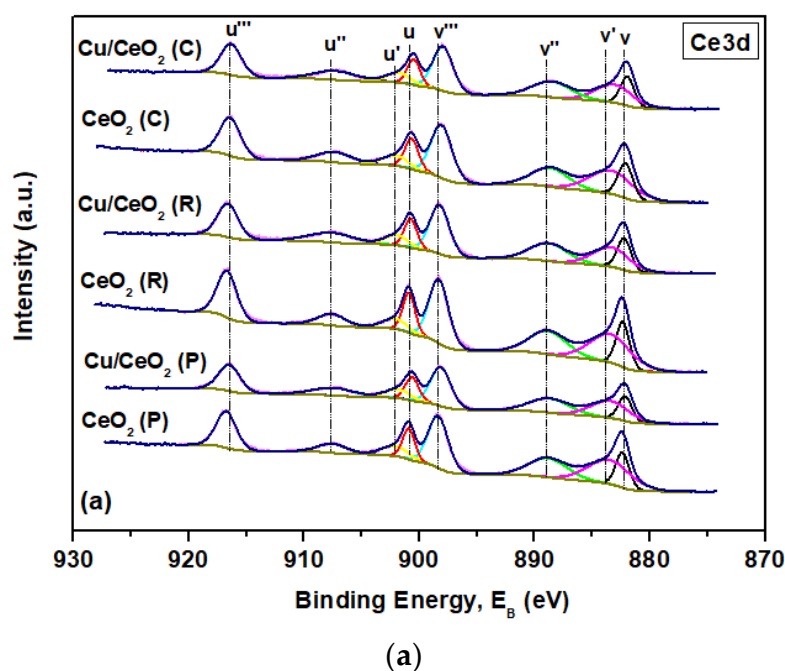
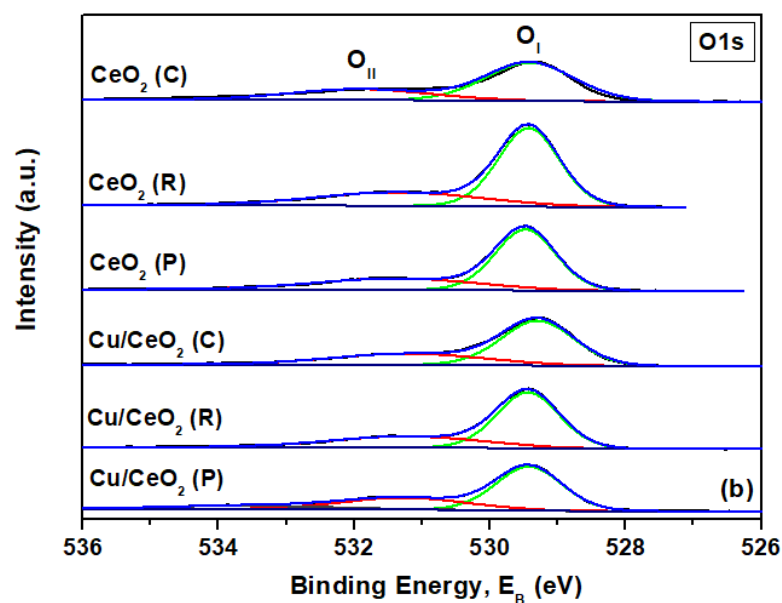
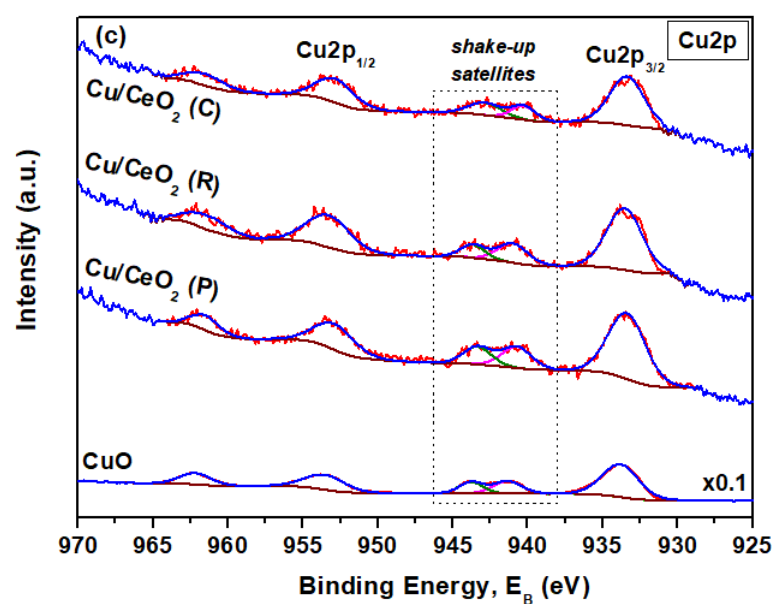


Figure 6. Cont.



(b)



(c)

Figure 6. XPS spectra of (a) Ce 3d, (b) O 1s and (c) Cu 2p of pure CeO₂ and CuO_x/CeO₂ samples.

Table 3. XPS data of pure CeO₂ and CuO_x/CeO₂ materials.

Sample	O _I /O _{II}	Ce ³⁺ (%)	Cu ⁺ (%)	Cu/Ce Atomic Ratio
CeO ₂ (C)	1.99	23.3	-	
CeO ₂ (P)	2.04	25.3	-	
CeO ₂ (R)	2.13	24.3	-	
Cu/CeO ₂ (C)	1.89	21.9	11.8	0.16
Cu/CeO ₂ (P)	1.96	23.3	13.0	0.35
Cu/CeO ₂ (R)	2.02	23.9	16.1	0.18

Figure 6b depicts the O 1s XPS spectra. The peak at 529.4 eV (O_I) is assigned to lattice oxygen, whereas the peak at 531.3 eV (O_{II}) is ascribed to oxygen chemisorbed, involving adsorbed O₂ (O⁻/O₂²⁻), adsorbed H₂O, OH⁻ and CO₃²⁻ species. In terms of the O_I/O_{II}

ratio, for pure ceria supports, the following order is found: CeO₂ (R) (2.13) > CeO₂ (P) (2.04) > CeO₂ (C) (1.99). Additionally, CuO_x/CeO₂ samples demonstrate the exact same trend, i.e., nanorods > nanopolyhedra > nanocubes, indicating the pivotal role of support morphology on oxygen species abundance. These findings, together with the TPR results, clearly imply that the rod-shaped materials exhibit the greatest abundance in labile oxygen species, leading to the superior reducibility and mobility of oxygen species.

The Cu 2p XPS spectra of the as-prepared Cu/CeO₂ samples are shown in Figure 6c, along with the spectrum of CuO (used as reference for comparison). All samples have two major peaks, namely Cu 2p_{1/2} (953.7 eV) and Cu2p_{3/2} (933.8 eV), along with shake-up satellites at 943 eV, characteristic of Cu²⁺ species [18,43,46], as further substantiated by the spectrum of CuO.

Due to difficulties in the resolution of the Cu⁺/Cu₂O and Cu²⁺/CuO species, the relative amount of Cu⁺ was obtained by the following equation (Equation (1)) [46–48]:

$$\%Cu^+ = (A - (A1/B)B)/(A + B) \times 100 \quad (1)$$

where A: area of the main Cu 2p_{3/2} peak; B: area of the shake-up peak; and A1/B: ratio of main/shake-up peaks for CuO (1.89).

The relative content of Cu⁺ in the CuO_x/CeO₂ samples is presented in Table 3. The Cu/CeO₂ (R) sample exhibits the largest amount of partially reduced copper species (16.1%), followed by nanopolyhedra (13.0%) and nanocubes (11.8%). This order totally coincides with the O_s/O_b ratio and reducibility order (Table 2), demonstrating the interrelationship between chemical state and redox properties. Specifically, the interaction between CuO_x species and ceria nanorods could lead to the stabilization of Cu⁺ species, leading to improved catalytic activity, as will be discussed in the sequence. Concerning the distribution of copper to the outer surface of CuO_x/CeO₂ samples, Cu/CeO₂ (C) and Cu/CeO₂ (R) show similar values of Cu/Ce surface atomic ratio, i.e., 0.16 and 0.18, respectively (Table 3), which is slightly lower than the nominal ratio (0.25). However, nanopolyhedra exhibit a Cu/Ce atomic ratio (0.35) higher than the nominal one, indicating the enrichment of catalyst surface to copper. These findings are in agreement with relevant literature studies [49], implying the significant effect of ceria morphology on the surface distribution of copper species.

2.6. Water–Gas Shift Reaction

The conversion of CO with temperature during the WGS reaction for CuO_x/CeO₂ materials is presented in Figure 7. At this point, it should be mentioned that pure ceria supports exhibit no catalytic activity in the whole temperature range investigated and therefore, they are not included in the figure. However, the impregnation of copper into ceria alters this behaviour considerably. It is clear that the support morphology affects the catalytic performance to a different extent. The rod-shaped sample shows the best catalytic behaviour in almost all temperature range tested, approaching the thermodynamic CO conversion at 350 °C. It ought to be mentioned that Cu/CeO₂ (P) loses its activity when it reaches 300 °C (i.e., equilibrium limitations associated with the exothermic WGS reaction prevailing over kinetic aspects), while Cu/CeO₂ (C) remains active throughout the entire temperature range investigated. Moreover, the stability of CuO_x/CeO₂ samples was tested at 350 °C for 22 h of time-on-stream (Figure 8). It is noteworthy that Cu/CeO₂ (R) exhibits superior stability (~82% CO conversion after 22 h), in contrast to the other two samples, which demonstrate a gradual deactivation. The latter could be tentatively ascribed to the agglomeration of Cu particles after WGS, which in turn could result in a decline of catalytic performance, in agreement with relevant studies [50,51]. In view of this fact, the XRD results for the used samples (not shown for brevity) revealed the formation of Cu phase with an average crystallite size following the order: 100 nm (P) > 70 nm (C) > 55 nm (R), in consistence with the deactivation sequence (Figure 7). Moreover, XPS analysis of the used samples revealed a Cu/Ce atomic ratio of 0.49, 0.41 and 0.36 for nanorods, nanocubes and nanopolyhedra, respectively, which is about threefold, twofold and onefold

compared to that of the as-prepared samples (Table 3). Interestingly, this order is inversely proportional to the copper crystallite size whereas coincides with the deactivation sequence, implying the key role of support morphology on the distribution of copper species. In view of this fact, the improved WGS stability of the rod-shaped sample could be attributed, inter alia, to their abundance in active copper sites on the catalyst surface under reaction conditions, as further discussed below.

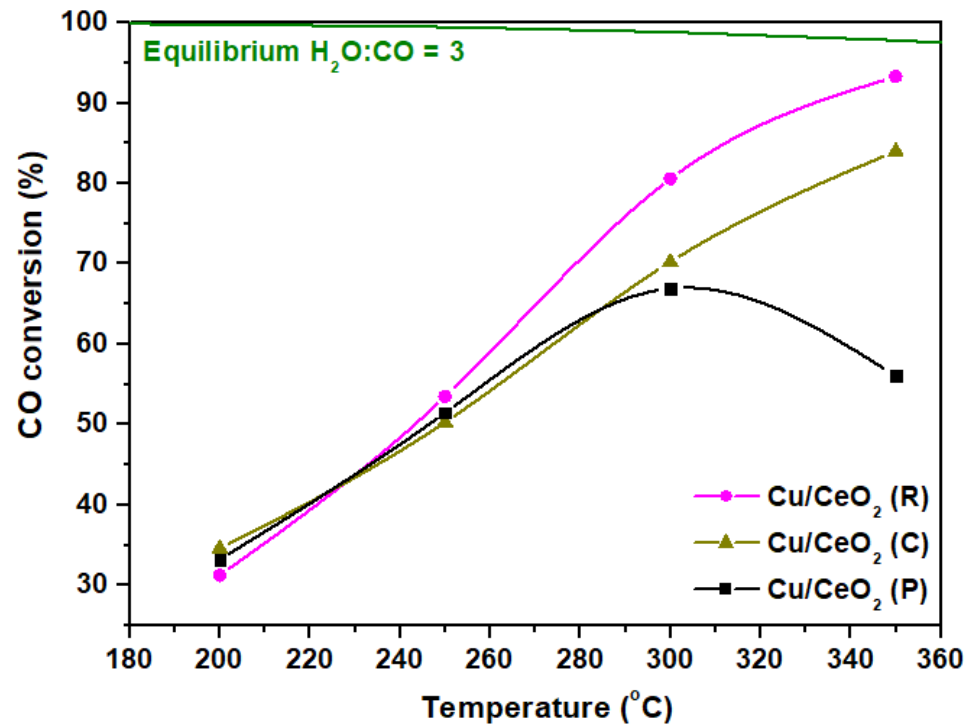


Figure 7. Conversion of CO with temperature for the $\text{CuO}_x/\text{CeO}_2$ samples. Reaction conditions: $\text{H}_2\text{O}:\text{CO} = 3$, $\text{WHSV} = 30,000 \text{ mL/g/h}$, $P = 1 \text{ bar}$.

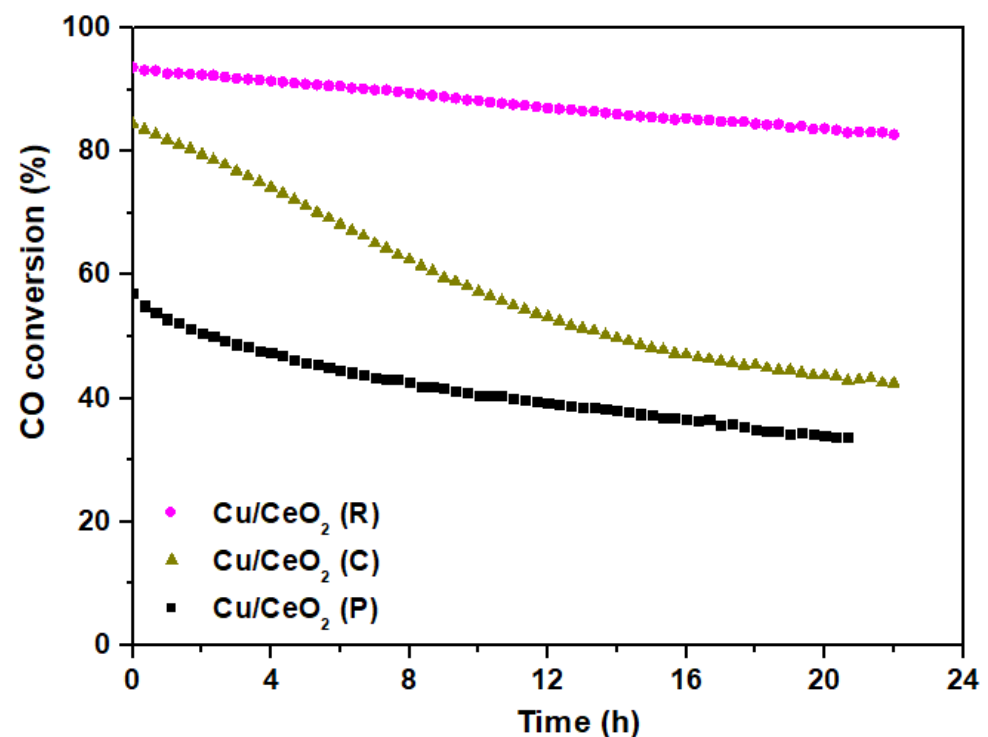


Figure 8. The conversion of CO as a function of time for the $\text{CuO}_x/\text{CeO}_2$ samples.

In particular, the superior WGS performance of Cu/CeO₂ (R) sample can be interpreted based on a well-established redox mechanism, which includes the following steps [22–24]:

- a. CO adsorption on the Cu⁺ active sites;
- b. Oxidation of CO from surface oxygen towards the formation of CO₂ and oxygen vacancy;
- c. Dissociation of H₂O on the oxygen vacancy and production of H₂;
- d. Re-oxidation of the support from H₂O.

In the above-mentioned mechanism, it is considered that the activation of water in the copper–ceria interface is the rate-determining step [23,26]. Moreover, on the ground of this mechanistic scheme, the formation of active oxygen species could be facilitated by the improved reducibility and oxygen mobility, whereas the synergistic interactions between copper and ceria can result in the stabilization of partially reduced Cu⁺ phases through the following redox equilibrium:



At this point, it is worth mentioning that different conclusions with regard to the effect of ceria morphology on the WGS performance of CuO_x/CeO₂ catalysts, have been previously drawn [28,29]. For instance, ceria nanooctahedrons were found to exhibit superior WGS activity by Ren et al. [28], as compared to nanorods and nanocubes, due to their abundance in highly dispersed copper species strongly interacting with ceria. However, in another study by Yao et al. [29], it was revealed that ceria nanospheres exhibit the best WGS activity/stability in comparison with nanorods and nanocubes due to their abundance in defects and imperfections, facilitating strong metal–support interactions and influenced copper dispersion and particle size. Interestingly, irrespective of ceria’s morphology, a close relationship between the catalytic activity and the relative abundance in oxygen vacancies and partially reduced copper species (Cu^{δ+}) was disclosed in both studies [28,29], in agreement with the present findings. The latter is of particular importance, revealing that the high WGS performance is closely related with the relative population of oxygen vacancies and the extent of metal–support interactions. However, various factors, such as support morphology, metal content, and synthesis procedure can exert a profound influence on intrinsic characteristics and metal–support interactions [19,20,32]. In view of this fact, the difference between the present work and the previous ones, in relation to the optimum ceria morphology, could be ascribed to the different loading, preparation procedure and pretreatment protocols. The key role of these parameters towards controlling the metal–support interactions and in turn the catalytic performance has been thoroughly reviewed [19,20,32].

On the basis of the present characterization studies, the rod-shaped samples (R), exposing {110}/{100} planes, exhibit the highest concentration of oxygen vacancies and defects, leading to enhanced oxygen kinetics and reducibility. Furthermore, the formation of surface active copper species (Cu⁺) is facilitated on ceria nanorods by Cu²⁺/Cu⁺ and Ce⁴⁺/Ce³⁺ redox equilibria (Equation (2)) [28]. Hence, the superior catalytic activity/stability of CeO₂ nanorods can be tentatively attributed to their abundance in oxygen vacancies and highly dispersed Cu⁺ species [23,26,52]. It should be noted, however, that further kinetic and operando studies are required for both as-prepared and used samples to better understand the improved WGS activity and stability of CuO_x/CeO₂ materials of rod-like morphology.

3. Materials and Methods

3.1. Reagents

All chemicals used were of analytical reagent grade. Ce(NO₃)₃·6H₂O (purity ≥ 99.0%, Fluka), Cu(NO₃)₂·2.5H₂O (purity 98.0%, Fluka, Bucharest, Romania) were precursors of the ceria and copper–ceria materials prepared. Ethanol (purity 99.8%, ACROS Organics,

Geel, Belgium), NaOH (purity $\geq 98\%$, Sigma-Aldrich, Taufkirchen, Germany) and double deionized water (DI) were also used for the synthesis.

3.2. Materials Synthesis

Initially, pure ceria nanoparticles of different morphology were obtained by a hydrothermal method by modifying the experimental conditions (NaOH concentration and/or aging temperature), as explicitly described in a previous work [27]. Then, the $\text{CuO}_x/\text{CeO}_2$ binary oxides were obtained by wet impregnation so as to yield a Cu/Ce ratio (atomic) of 0.25, which corresponds to ca. 8.5 wt.% Cu [27]. The single ceria materials are hereafter called as CeO_2 (P), CeO_2 (R), CeO_2 (C), referring to nanopolyhedra, nanorods and nanocubes, respectively. The general term “ CuO_x ” is used throughout the text to denote the multivalence states of copper. The $\text{CuO}_x/\text{CeO}_2$ mixed oxides of different nanostructure are designated, for clarity’s sake, as Cu/ CeO_2 (P), Cu/ CeO_2 (R), Cu/ CeO_2 (C).

3.3. Materials Characterization

The obtained materials were characterized by several techniques, including N_2 adsorption-desorption at -196°C , X-ray diffraction (XRD, Siemens D500, Munich, Germany), H_2 -temperature programmed reduction (TPR, AMI-200 Catalyst Characterization Instrument, Altamira Instruments, Pittsburgh, PA, USA), transmission electron microscopy (TEM, Leo 906 E apparatus, Austin, TX, USA) and X-ray photoelectron spectroscopy (XPS, Kratos AXIS Ultra HSA, Manchester, United Kingdom), as elaborated in our previous works [27,53]. Additionally, the samples were characterized by ultraviolet-visible spectroscopy (UV-Vis) on a Perkin Elmer LAMBDA 950 in the wavelength range of 250–2500 nm. The actual metal loading was determined by Inductively Coupled Plasma Atomic Emission Spectroscopy (ICP-AES) in a Perkin-Elmer Optima 4300DV apparatus. In particular, Scherrer’s equation (Equation (3)) was employed to determine the primary particle size of a given crystal phase based on the most intense diffraction peak of CeO_2 (2θ : 28.5° and 47.6°) and CuO (2θ : $\sim 35.3^\circ$ and 38.2°) patterns:

$$D_{\text{XRD}} = \frac{K \cdot \lambda}{\beta \cdot \cos \theta} \quad (3)$$

where K is the Scherrer constant; λ is the wavelength of the X-ray in nm; β is the line broadening; θ is the Bragg angle [54].

3.4. Catalytic Evaluation Studies

Activity measurements were carried out in a fixed-bed reactor. This reactor consisted of a stainless-steel tube with a length of 60 mm and 10 mm o.d., loaded with 0.2 g of catalyst diluted with glass beads and framed in both ends by two discs of stainless-steel mesh.

Prior to the WGS tests, the catalyst was reduced at 200°C for 1 h using a mixture of 10 vol.% of H_2 in N_2 . After reduction, 100 mL/min of N_2 was used for 30 min to sweep H_2 from the system. The catalytic tests were performed with a total flow rate of 100 mL/min, a feed composition of 5 vol.% CO, 15 vol.% H_2O (CO: H_2O = 3) balanced with N_2 (weight hourly space velocity: WHSV = 30,000 mL/g/h) at atmospheric pressure, and temperatures ranging from 200 to 350°C .

The gases were fed by means of mass flow controllers (Bronkhorst High-Tech B.V., Ruurlo, Netherlands). A Controlled Evaporation and Mixing (CEM, Bronkhorst High-Tech B.V., Ruurlo, Netherlands) unit was used to evaporate the water while mixing the generated steam with the feed gases. The reactor was placed in the middle of a three zone cylindrical electric oven (from Termolab, Águeda, Portugal), each one equipped with a separate PID programmable temperature controller (from Shimaden, Tokyo, Japan). The temperature of the bed was measured using a type K thermocouple inserted in direct contact with the catalyst bed. The steam present in the outlet stream was condensed using a Peltier cooler placed at the reactor output. More details about the set-up are available at [55].

The dry product gases were analysed with an Agilent (model 7820A) gas chromatograph equipped with two detectors (TCD and FID, California, United States) and two

columns (Plot Q (30 m × 0.32 mm) and Plot 5A (30 m × 0.32 mm)). The H₂ was analysed by TCD with argon as carrier gas to achieve a better response for hydrogen owing to the higher difference in thermal conductivity. The carbon balance was close to 100% in all the tests carried out in this work.

The catalytic activity was expressed as a percentage of CO conversion calculated as:

$$X_{\text{CO}}(\%) = \frac{F_{\text{CO}}^{\text{in}} - F_{\text{CO}}^{\text{out}}}{F_{\text{CO}}^{\text{in}}} \times 100 \quad (4)$$

where $F_{\text{CO}}^{\text{in}}$ and $F_{\text{CO}}^{\text{out}}$ stand for the CO molar flow rate at the reactor inlet and outlet, respectively. The CO conversion in the equilibrium was determined by the Gibbs free energy minimization method with the Aspen plus software as described elsewhere [56].

4. Conclusions

Three different ceria nanoshapes (nanopolyhedra (P), nanocubes (C) and nanorods (R)) were used as supports for Cu catalysts in the WGS reaction. A thorough characterization study was employed to better understand the morphology effects of CeO₂ on the physicochemical properties and the WGS activity of CuO_x/CeO₂ mixed oxides. The data unequivocally show the importance of the support morphology on the redox/surface properties and thus on the catalytic activity. Bare ceria supports are inactive in all temperature range tested, whereas addition of copper into ceria alters this behaviour significantly, according to the order: Cu/CeO₂ (R) > Cu/CeO₂ (C) > Cu/CeO₂ (P). The superior catalytic performance of CuO_x/CeO₂ nanorods, in terms of conversion/stability, could be mainly ascribed to their abundance in labile oxygen species and surface copper species, resulting in enhanced reducibility, oxygen exchange kinetics and highly active copper species (Cu⁺), on account of a redox-type mechanism.

Author Contributions: M.L. contributed to materials synthesis, results interpretation and paper writing; S.S. and S.A.C.C. contributed to materials characterizations; M.A.S. and L.M.M. contributed to catalytic evaluation studies; M.K. conceptualized the overall idea of this research, validated the results and administered the project. Finally, M.K. reviewed, edited and submitted the manuscript in the final form. All authors have read and agreed to the published version of the manuscript.

Funding: This research has been co-financed by the European Union and Greek national funds through the Operational Program Competitiveness, Entrepreneurship and Innovation, under the call RESEARCH-CREATE-INNOVATE (project code: T1EDK-00094). This work was partially supported by Base Funding-UIDB/EQU/50020/2020 of the Associate Laboratory LSRE-LCM- and UIDB/00511/2020 of the Laboratory for Process Engineering, Environment, Biotechnology and Energy-LEPABE-funded by national funds through FCT/MCTES (PIDDAC). This work was also supported by national funds through FCT, under the Scientific Employment Stimulus-Institutional Call (CEECINST/00102/2018) and partially supported by the Associate Laboratory for Green Chemistry—LAQV, financed by national funds from FCT/MCTES (UIDB/50006/2020 and UIDP/50006/2020). M. A. Soria also thanks the FCT for the financial support of his work contract through the Scientific Employment Support Program (Norma Transitória DL 57/2017).

Data Availability Statement: Data is contained within the article.

Acknowledgments: Authors thank Carlos Sá (CEMUP) for the assistance with XPS analyses.

Conflicts of Interest: The authors declare no conflict of interest.

References

1. Ebrahimi, P.; Kumar, A.; Khraisheh, M. A review of recent advances in water-gas shift catalysis for hydrogen production. *Emergent Mater.* **2020**, *3*, 881–917. [[CrossRef](#)]
2. Navarro, R.M.; Peña, M.A.; Fierro, J.L.G. Hydrogen production reactions from carbon feedstocks: Fossil fuels and biomass. *Chem. Rev.* **2007**, *107*, 3952–3991. [[CrossRef](#)]
3. Andrews, J.; Shabani, B. Re-envisioning the role of hydrogen in a sustainable energy economy. *Int. J. Hydrogen Energy* **2012**, *37*, 1184–1203. [[CrossRef](#)]

4. Rodrigues, A.E.; Madeira, L.M.; Wu, Y.-J.; Faria, R. *Sorption Enhanced Reaction Processes*; World Scientific Publishing Europe Ltd.: 57 Shelton Street, Covent Garden, London, UK, 2018; ISBN 9781786343567. [[CrossRef](#)]
5. Pal, D.B.; Chand, R.; Upadhyay, S.N.; Mishra, P.K. Performance of water gas shift reaction catalysts: A review. *Renew. Sustain. Energy Rev.* **2018**, *93*, 549–565. [[CrossRef](#)]
6. Tao, F.; Ma, Z. Water-gas shift on gold catalysts: Catalyst systems and fundamental studies. *Phys. Chem. Chem. Phys.* **2013**, *15*, 15260–15270. [[CrossRef](#)] [[PubMed](#)]
7. Sun, C.; Xue, D. Size-dependent oxygen storage ability of nano-sized ceria. *Phys. Chem. Chem. Phys.* **2013**, *15*, 14414–14419. [[CrossRef](#)] [[PubMed](#)]
8. Montini, T.; Melchionna, M.; Monai, M.; Fornasiero, P. Fundamentals and catalytic applications of CeO₂-based materials. *Chem. Rev.* **2016**, *116*, 5987–6041. [[CrossRef](#)] [[PubMed](#)]
9. Monte, M.; Munuera, G.; Costa, D.; Conesa, J.C.; Martínez-Arias, A. Near-ambient XPS characterization of interfacial copper species in ceria-supported copper catalysts. *Phys. Chem. Chem. Phys.* **2015**, *17*, 29995–30004. [[CrossRef](#)]
10. Sayle, T.X.T.; Caddeo, F.; Zhang, X.; Sakthivel, T.; Das, S.; Seal, S.; Ptasinska, S.; Sayle, D.C. Structure-activity map of ceria nanoparticles, nanocubes, and mesoporous architectures. *Chem. Mater.* **2016**, *28*, 7287–7295. [[CrossRef](#)]
11. Zabilskiy, M.; Djinić, P.; Tchernychova, E.; Pintar, A. N₂O decomposition over CuO/CeO₂ catalyst: New insights into reaction mechanism and inhibiting action of H₂O and NO by operando techniques. *Appl. Catal. B Environ.* **2016**, *197*, 146–158. [[CrossRef](#)]
12. Zabilskiy, M.; Djinić, P.; Tchernychova, E.; Tkachenko, O.P.; Kustov, L.M.; Pintar, A. Nanoshaped CuO/CeO₂ materials: Effect of the exposed ceria surfaces on catalytic activity in N₂O decomposition reaction. *ACS Catal.* **2015**, *5*, 5357–5365. [[CrossRef](#)]
13. Singha, R.K.; Shukla, A.; Yadav, A.; Sivakumar Konathala, L.N.; Bal, R. Effect of metal-support interaction on activity and stability of Ni-CeO₂ catalyst for partial oxidation of methane. *Appl. Catal. B Environ.* **2017**, *202*, 473–488. [[CrossRef](#)]
14. Wu, Z.; Li, M.; Howe, J.; Meyer, H.M., III; Overbury, S.H. Probing defect sites on CeO₂ nanocrystals with well-defined surface planes by Raman spectroscopy and O₂ adsorption. *Langmuir* **2010**, *26*, 16595–16606. [[CrossRef](#)]
15. Zhou, Y.; Chen, A.; Ning, J.; Shen, W. Electronic and geometric structure of the copper-ceria interface on Cu/CeO₂ catalysts. *Chin. J. Catal.* **2020**, *41*, 928–937. [[CrossRef](#)]
16. Cargnello, M.; Doan-Nguyen, V.V.T.; Gordon, T.R.; Diaz, R.E.; Stach, E.A.; Gorte, R.J.; Fornasiero, P.; Murray, C.B. Control of metal nanocrystal size reveals metal-support interface role for ceria catalysts. *Science* **2013**, *341*, 771–773. [[CrossRef](#)]
17. Qiu, N.; Zhang, J.; Wu, Z. Peculiar surface-interface properties of nanocrystalline ceria-cobalt oxides with enhanced oxygen storage capacity. *Phys. Chem. Chem. Phys.* **2014**, *16*, 22659–22664. [[CrossRef](#)]
18. Konsolakis, M.; Carabineiro, S.A.C.; Papista, E.; Marnellos, G.E.; Tavares, P.B.; Agostinho Moreira, J.; Romaguera-Barcelay, Y.; Figueiredo, J.L. Effect of preparation method on the solid state properties and the deN₂O performance of CuO–CeO₂ oxides. *Catal. Sci. Technol.* **2015**, *5*, 3714–3727. [[CrossRef](#)]
19. Konsolakis, M. The role of Copper–Ceria interactions in catalysis science: Recent theoretical and experimental advances. *Appl. Catal. B Environ.* **2016**, *198*, 49–66. [[CrossRef](#)]
20. Konsolakis, M.; Lykaki, M. Recent advances on the rational design of non-precious metal oxide catalysts exemplified by CuO_x/CeO₂ binary system: Implications of size, shape and electronic effects on intrinsic reactivity and metal-support interactions. *Catalysts* **2020**, *10*, 160. [[CrossRef](#)]
21. Zhao, G.-C.; Wang, J.-S.; Qiu, Y.-Q.; Liu, C.-G. Ensemble effect of heterogeneous Cu atoms promoting water-gas shift reaction. *Mol. Catal.* **2020**, *493*, 111046. [[CrossRef](#)]
22. Saeidi, S.; Fazlollahi, F.; Najari, S.; Iranshahi, D.; Klemeš, J.J.; Baxter, L.L. Hydrogen production: Perspectives, separation with special emphasis on kinetics of WGS reaction: A state-of-the-art review. *J. Ind. Eng. Chem.* **2017**, *49*, 1–25. [[CrossRef](#)]
23. Chen, A.; Yu, X.; Zhou, Y.; Miao, S.; Li, Y.; Kuld, S.; Sehested, J.; Liu, J.; Aoki, T.; Hong, S.; et al. Structure of the catalytically active copper–ceria interfacial perimeter. *Nat. Catal.* **2019**, *2*, 334–341. [[CrossRef](#)]
24. Mudiyansele, K.; Senanayake, S.D.; Feria, L.; Kundu, S.; Baber, A.E.; Graciani, J.; Vidal, A.B.; Agnoli, S.; Evans, J.; Chang, R.; et al. Importance of the metal-oxide interface in catalysis: In situ studies of the water-gas shift reaction by ambient-pressure X-ray photoelectron spectroscopy. *Angew. Chem. Int. Ed.* **2013**, *52*, 5101–5105. [[CrossRef](#)]
25. Si, R.; Raitano, J.; Yi, N.; Zhang, L.; Chan, S.-W.; Flytzani-Stephanopoulos, M. Structure sensitivity of the low-temperature water-gas shift reaction on Cu-CeO₂ catalysts. *Catal. Today* **2012**, *180*, 68–80. [[CrossRef](#)]
26. Ning, J.; Zhou, Y.; Shen, W. Atomically dispersed copper species on ceria for the low-temperature water-gas shift reaction. *Sci. China Chem.* **2020**, 1–8. [[CrossRef](#)]
27. Lykaki, M.; Pachatouridou, E.; Carabineiro, S.A.C.; Iliopoulou, E.; Andriopoulou, C.; Kallithrakas-Kontos, N.; Boghosian, S.; Konsolakis, M. Ceria nanoparticles shape effects on the structural defects and surface chemistry: Implications in CO oxidation by Cu/CeO₂ catalysts. *Appl. Catal. B Environ.* **2018**, *230*, 18–28. [[CrossRef](#)]
28. Ren, Z.; Peng, F.; Li, J.; Liang, X.; Chen, B. Morphology-dependent properties of Cu/CeO₂ catalysts for the water-gas shift reaction. *Catalysts* **2017**, *7*, 48. [[CrossRef](#)]
29. Yao, S.Y.; Xu, W.Q.; Johnston-Peck, A.C.; Zhao, F.Z.; Liu, Z.Y.; Luo, S.; Senanayake, S.D.; Martínez-Arias, A.; Liu, W.J.; Rodriguez, J.A. Morphological effects of the nanostructured ceria support on the activity and stability of CuO/CeO₂ catalysts for the water-gas shift reaction. *Phys. Chem. Chem. Phys.* **2014**, *16*, 17183–17195. [[CrossRef](#)]
30. Agarwal, S.; Zhu, X.; Hensen, E.J.M.; Mojet, B.L.; Lefferts, L. Surface-dependence of defect chemistry of nanostructured ceria. *J. Phys. Chem. C* **2015**, *119*, 12423–12433. [[CrossRef](#)]

31. Zhang, Z.; Wang, S.-S.; Song, R.; Cao, T.; Luo, L.; Chen, X.; Gao, Y.; Lu, J.; Li, W.-X.; Huang, W. The most active Cu facet for low-temperature water gas shift reaction. *Nat. Commun.* **2017**, *8*, 488. [[CrossRef](#)]
32. Konsolakis, M.; Lykaki, M. Facet-dependent reactivity of ceria nanoparticles exemplified by CeO₂-based transition metal catalysts: A critical review. *Catalysts* **2021**, *11*, 452. [[CrossRef](#)]
33. Allwar, A.; Md Noor, A.; Nawi, M. Textural characteristics of activated carbons prepared from oil palm shells activated with ZnCl₂ and pyrolysis under nitrogen and carbon dioxide. *J. Phys. Sci.* **2008**, *19*, 93–104.
34. Tan, L.; Tao, Q.; Gao, H.; Li, J.; Jia, D.; Yang, M. Preparation and catalytic performance of mesoporous ceria-base composites CuO/CeO₂, Fe₂O₃/CeO₂ and La₂O₃/CeO₂. *J. Porous Mater.* **2017**, *24*, 795–803. [[CrossRef](#)]
35. Anushree; Kumar, S.; Sharma, C. Synthesis, characterization and catalytic wet air oxidation property of mesoporous Ce_{1-x}Fe_xO₂ mixed oxides. *Mater. Chem. Phys.* **2015**, *155*, 223–231. [[CrossRef](#)]
36. Farahmandjou, M.; Zarinkamar, M. Synthesis of nano-sized ceria (CeO₂) particles via a cerium hydroxy carbonate precursor and the effect of reaction temperature on particle morphology. *J. Ultrafine Grained Nanostruct. Mater.* **2015**, *48*, 5–10. [[CrossRef](#)]
37. Ren, Z.; Peng, F.; Chen, B.; Mei, D.; Li, J. A combined experimental and computational study of water-gas shift reaction over rod-shaped Ce_{0.75}M_{0.25}O₂ (M = Ti, Zr, and Mn) supported Cu catalysts. *Int. J. Hydrogen Energy* **2017**, *42*, 30086–30097. [[CrossRef](#)]
38. Pastor-Pérez, L.; Ramos-Fernández, E.V.; Sepúlveda-Escribano, A. Effect of the CeO₂ synthesis method on the behaviour of Pt/CeO₂ catalysis for the water-gas shift reaction. *Int. J. Hydrogen Energy* **2019**, *44*, 21837–21846. [[CrossRef](#)]
39. Lykaki, M.; Pachatouridou, E.; Iliopoulou, E.; Carabineiro, S.A.C.; Konsolakis, M. Impact of the synthesis parameters on the solid state properties and the CO oxidation performance of ceria nanoparticles. *RSC Adv.* **2017**, *7*, 6160–6169. [[CrossRef](#)]
40. Liu, J.; Zhao, Z.; Wang, J.; Xu, C.; Duan, A.; Jiang, G.; Yang, Q. The highly active catalysts of nanometric CeO₂-supported cobalt oxides for soot combustion. *Appl. Catal. B Environ.* **2008**, *84*, 185–195. [[CrossRef](#)]
41. Aboukais, A.; Skaf, M.; Hany, S.; Cousin, R.; Aouad, S.; Labaki, M.; Abi-Aad, E. A comparative study of Cu, Ag and Au doped CeO₂ in the total oxidation of volatile organic compounds (VOCs). *Mater. Chem. Phys.* **2016**, *177*, 570–576. [[CrossRef](#)]
42. Zhu, P.; Li, J.; Huang, Q.; Yan, S.; Liu, M.; Zhou, R. High performance CuO-CeO₂ catalysts for selective oxidation of CO in excess hydrogen: Effect of hydrothermal preparation conditions. *J. Nat. Gas Chem.* **2009**, *18*, 346–353. [[CrossRef](#)]
43. Guo, X.; Zhou, R. A new insight into the morphology effect of ceria on CuO/CeO₂ catalysts for CO selective oxidation in hydrogen-rich gas. *Catal. Sci. Technol.* **2016**, *6*, 3862–3871. [[CrossRef](#)]
44. Sundar, R.S.; Deevi, S. CO oxidation activity of Cu-CeO₂ nano-composite catalysts prepared by laser vaporization and controlled condensation. *J. Nanopart. Res.* **2006**, *8*, 497–509. [[CrossRef](#)]
45. Jampa, S.; Wangkawee, K.; Tantisiyanurak, S.; Changpradit, J.; Jamieson, A.M.; Chaisuwan, T.; Luengnaruemitchai, A.; Wongkasemjit, S. High performance and stability of copper loading on mesoporous ceria catalyst for preferential oxidation of CO in presence of excess of hydrogen. *Int. J. Hydrogen Energy* **2016**, *42*, 5537–5548. [[CrossRef](#)]
46. Carabineiro, S.A.C.; Konsolakis, M.; Marnellos, G.E.N.; Asad, M.F.; Soares, O.S.G.P.; Tavares, P.B.; Pereira, M.F.R.; De Melo Órfão, J.J.; Figueiredo, J.L. Ethyl acetate abatement on copper catalysts supported on ceria doped with rare earth oxides. *Molecules* **2016**, *21*, 644. [[CrossRef](#)]
47. Biesinger, M.C.; Hart, B.R.; Polack, R.; Kobe, B.A.; Smart, R.S.C. Analysis of mineral surface chemistry in flotation separation using imaging XPS. *Miner. Eng.* **2007**, *20*, 152–162. [[CrossRef](#)]
48. Biesinger, M.C.; Lau, L.W.M.; Gerson, A.R.; Smart, R.S.C. Resolving surface chemical states in XPS analysis of first row transition metals, oxides and hydroxides: Sc, Ti, V, Cu and Zn. *Appl. Surf. Sci.* **2010**, *257*, 887–898. [[CrossRef](#)]
49. Cui, Y.; Dai, W.-L. Support morphology and crystal plane effect of Cu/CeO₂ nanomaterial on the physicochemical and catalytic properties for carbonate hydrogenation. *Catal. Sci. Technol.* **2016**, *6*, 7752–7762. [[CrossRef](#)]
50. Wang, X.; Liu, Y.; Peng, X.; Lin, B.; Cao, Y.; Jiang, L. Sacrificial adsorbate strategy achieved strong metal-support interaction of stable Cu nanocatalysts. *ACS Appl. Energy Mater.* **2018**, *1*, 1408–1414. [[CrossRef](#)]
51. Jeong, D.-W.; Na, H.-S.; Shim, J.-O.; Jang, W.-J.; Roh, H.-S.; Jung, U.H.; Yoon, W.L. Hydrogen production from low temperature WGS reaction on co-precipitated Cu-CeO₂ catalysts: An optimization of Cu loading. *Int. J. Hydrogen Energy* **2014**, *39*, 9135–9142. [[CrossRef](#)]
52. Zhao, F.; Liu, Z.; Xu, W.; Yao, S.; Si, R.; Johnston-Peck, A.C.; Martínez-Arias, A.; Hanson, J.C.; Senanayake, S.D.; Rodriguez, J.A. Pulse studies to decipher the role of surface morphology in CuO/CeO₂ nanocatalysts for the water gas shift reaction. *Catal. Lett.* **2015**, *145*, 808–815. [[CrossRef](#)]
53. Konsolakis, M.; Lykaki, M.; Stefa, S.; Carabineiro, S.A.C.; Varvoutis, G.; Papista, E.; Marnellos, G.E. CO₂ hydrogenation over nanoceria-supported transition metal catalysts: Role of ceria morphology (nanorods versus nanocubes) and active phase nature (Co versus Cu). *Nanomaterials* **2019**, *9*, 1739. [[CrossRef](#)] [[PubMed](#)]
54. Saitzek, S.; Blach, J.-F.; Villain, S.; Gavarrri, J.-R. Nanostructured ceria: A comparative study from X-ray diffraction, Raman spectroscopy and BET specific surface measurements. *Phys. Stat. Sol.* **2008**, *205*, 1534–1539. [[CrossRef](#)]
55. Soria, M.A.; Rocha, C.; Tosti, S.; Mendes, A.; Madeira, L.M. CO_x free hydrogen production through water-gas shift reaction in different hybrid multifunctional reactors. *Chem. Eng. J.* **2019**, *356*, 727–736. [[CrossRef](#)]
56. Parente, M.; Soria, M.A.; Madeira, L.M. Hydrogen and/or syngas production through combined dry and steam reforming of biogas in a membrane reactor: A thermodynamic study. *Renew. Energy* **2020**, *157*, 1254–1264. [[CrossRef](#)]